CrossMark

ORIGINAL ARTICLE

Optimal structural design of a Biglide parallel drill grinder

Guanglei Wu[1,2]

Abstract This paper deals with the optimal structural design of a Biglide parallel grinder for drill grinding. A pair of spatial modules is adopted to replace the conventional parallelogram to enhance the out-of-plane stiffness of the latter. A multi-objective design optimization problem is formulated, of which the stiffness, motion/force transmission, and work space are taken into consideration. The Pareto front of the optimization problem is obtained to provide the optimum design of the Biglide machine, and a scatter matrix is visualized to reveal the influence of the link dimensions to the performance. The selected design from the Pareto front guarantees the requirement on the elastostatic performance in the grinding process with increased dexterous workspace size.

Keywords Biglide parallel grinder · Structural design · Multi-objective optimization · Pareto front · Cartesian stiffness matrix

1 Introduction

Drilling is one of the most important and frequently performed manufacturing process, which comprises approximately

✉ Guanglei Wu
gwu@dlut.edu.cn

1 School of Mechanical Engineering, Dalian University of Technology, 116024 Dalian, China

2 Department of Mechanical and Manufacturing Engineering, Aalborg University, 9220 Aalborg, Denmark

30 % of the material removal process. The drills play a significant role in the drilling operation, of which the drill point geometry is the most important part as it heavily influences the accuracy of the hole during the machining process [1]. Sharpening the drill point, such as twist or helical drill, requires a special drill grinder that produces three-axis motion simultaneously. In light of this purpose, a parallel mechanism (PM)-based Biglide grinder [2], as shown in Fig. 1, was proposed for drill grinding, despite its small workspace (WS), as the drill point grinder does not require a big workspace [3]. Thanks to the unique motion characteristics of this Biglide parallel mechanism, the drill grinding can be achieved by two-axis motion instead with this machine [4].

Upon the investigation of the stiffness behavior [5], the stiffness along the normal to the motion of the planar Biglide mechanism can be improved with an alternative lightweight design towards high dynamic response. Moreover, with the requirement of dexterity for grinding complicated drill point geometry, an operational dexterous workspace of the machine in Fig. 1 needs to be improved. This study aims at the optimum structural design of the Biglide parallel grinder in order to enlarge its dexterous workspace without significantly increased mass in motion.

In general, the structural optimization usually simultaneously deals with the kinematic and kinetostatic/dynamic aspects, both of which include a number of performance measures that essentially vary throughout the workspace. For the kinematic performance, the characteristics of the workspace that reflect the shape, size, and presence of singularities are of primary importance in the PM design [6]. The workspace optimization of parallel manipulators

can usually be solved by means of two different formulations. The first formulation aims to design a manipulator whose workspace contains a prescribed workspace, and the second approach aims to design a manipulator of which the workspace is as large as possible. However, maximizing the manipulator workspace may result in a poor design with regard to the manipulator dexterity/manipulability [7], which is another utmost important concern to map the motion/force [8] between the actuators and end-effector. This problem can be solved by properly defining the constraints of the optimization problem. Here, the optimization problem of the Biglide machine is based on the first formulation, namely, the dimensional design of the mechanism subject to a prescribed workspace.

Compared to kinematic aspects, the kinetostatic/dynamic aspects are more complex as the latter requires a detailed description of the mechanism structure and the evaluation is usually time consuming. Of the kinetostatic aspects, stiffness is particularly of importance, since it is a measure of the ability of its end-effector to resist deformation due to an external wrench (forces and moments), which can be predicted by means of the computation of the stiffness matrix [9]. Therefore, the design of parallel kinematic machines is a complex subject, wherein the fundamental problem is that their performance heavily depends on their geometry [10] and the mutual dependency of almost all the performance measures. This makes the problem computationally complex and yields the traditional solution approaches inefficient [11], wherefrom an efficient approach is to adopt the multi-objective optimization method. As the objective functions are usually antagonistic, no single solution can be achieved in this process. The solutions of such a problem are non-dominated solutions, also called Pareto optimal solutions. In the literature, various approaches of multi-objective design optimization to consider kinematic,

dynamic, and static criteria have been applied to different types of PMs [12–17]. In these works, workspace, global condition index (GCI), eigenfrequency, and actuator torque have been widely used as objective functions and constraints, where the transmission/pressure angle of PMs is rarely considered. Besides, the thermal stability and machining dynamics should also be taken into account when the machine tool is deployed in high-speed machining [18, 19].

This paper deals with the optimal structural design of the Biglide parallel grinder introduced in Fig. 1. A pair of spatial modules, composed of composite carbon fiber tubes, is adopted to replace the parallelogram for the lightweight design. A multi-objective design optimization problem is formulated, where the stiffness, motion/force transmission, and workspace are taken into consideration. The Pareto front of the optimization problem is obtained to provide the optimum design of the Biglide machine, and a scatter matrix is visualized to reveal the influence of the link dimensions to the performance. The selected design from the Pareto front guarantees the requirement on the elastostatic performance with increased workspace size.

2 Architecture of the Biglide mechanism

The drill grinder is based on a serial-parallel Biglide parallel mechanism [2] as displayed in Fig. 2a, which has a decoupled translation along the normal to the plane of parallel mechanism's motion. The part of parallel mechanism, a two degree-of-freedom (2-dof) planar translational PM, is consisted of a pair of spatial modules connected to the mobile platform (MP) and two sliding units, where the sliding unit is actuated via lead screw system. The pair of spatial modules constrains the mechanism to generate planar 2-dof translation, which are equivalent to the structure of
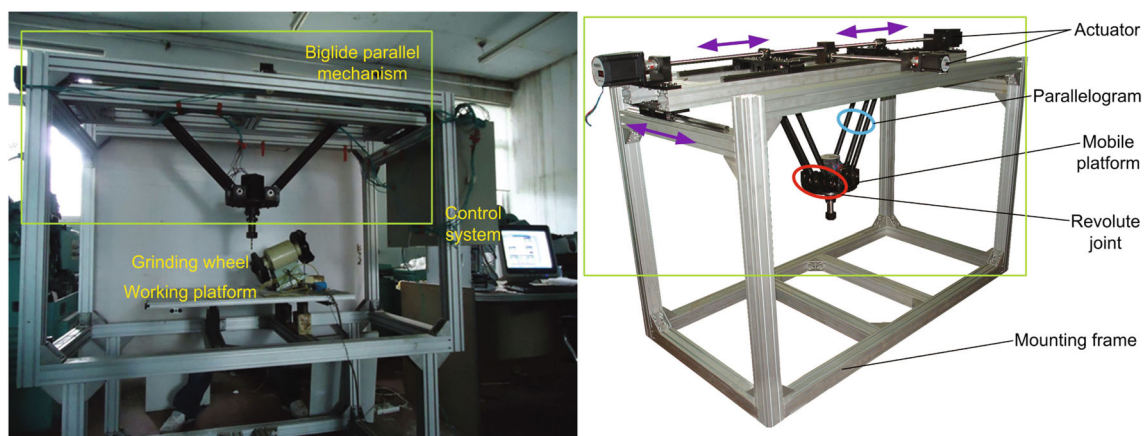

Fig. 1 Prototype of the grinding machine based on the Biglide parallel mechanism
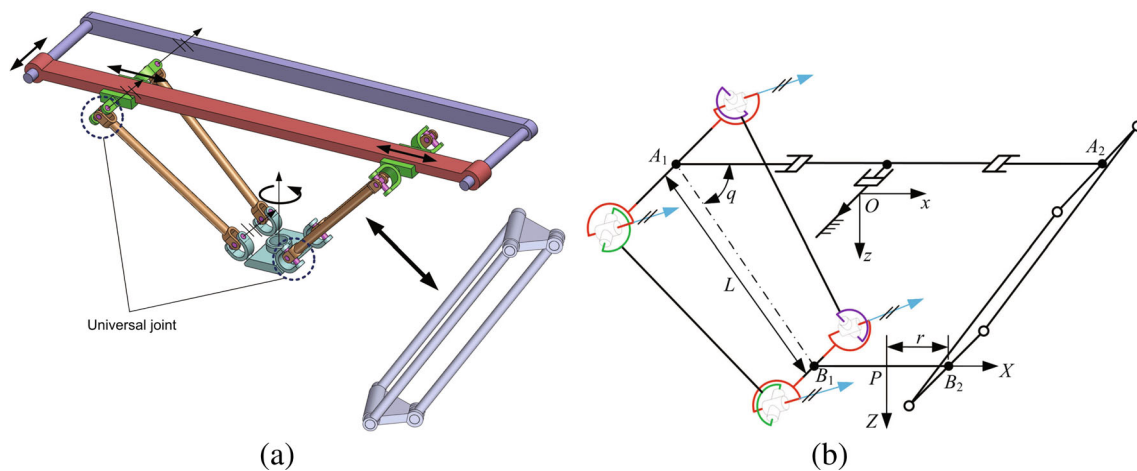
Fig. 2 The Biglide parallel mechanism. **a** Simplified CAD model. **b** Kinematic structure

parallelograms [5, 20]. Thus, this hybrid mechanism produces 3-dof translation. Moreover, with an additional actuator attached to the mobile platform, its end-effector can generate a rotation around the vertical axis, which can be well adapted to twist or helical drill grinding.

Figure 2b depicts the kinematic structure of the Biglide parallel mechanism. A reference coordinate frame (x, y, z) is built on the top of the mounting frame, with the origin O located at the geometric center. The x-axis is parallel to segment $A_1 A_2$ and z-axis is parallel to the vertical axis pointing downwards. A moving frame (X, Y, Z) is attached to the mobile platform, with the origin P located at the geometric center, of which the coordinate axes are parallel to those of the reference frame. The Cartesian coordinate of point A_i in the frame (x, y, z) is denoted by $(a_i, y, 0)$.

3 Elastostatic analysis of the Biglide machine

The Biglide parallel mechanism is to be used as a machine tool for drill grinding, wherein the stiffness behavior is of importance as the stiffness strongly influences the positioning and orientational accuracies. An efficient method to predict the stiffness of a manipulator is to compute and characterize its stiffness matrix. A widely adopted approach to model the stiffness matrix of PMs is the virtual joint method (VJM) [21–25], i.e., the lumped modeling, since it provides acceptable accuracy in short computational time.

3.1 Cartesian stiffness matrix of the machine

In order to evaluate the influence of the geometric parameters of the manipulator architecture and the link dimensions

as well as the end-effector position/orientation to the manipulator stiffness, an analytical stiffness modeling approach is essential to calculate the stiffness matrix of the manipulator, in which the analytical model can be readily used for manipulator parameterization and design optimization [26, 27]. Here, the stiffness model is established with the virtual-spring approach [25] based on the screw coordinates [28], as this approach considers the actuator/link deflections and the influence of the passive joints simultaneously to provide high computation accuracy with less time consumption. Moreover, the stiffness matrix is computed under the assumption that the manipulator is in unloaded equilibrium with rigid base and mobile platforms and frictionless joints; thus, the manipulator stiffness is subject to the stiffnesses of actuators and limbs.

3.1.1 Actuation stiffness

The translation of the sliding unit of the machine is realized through the lead screw system. For a lead screw actuation system, let K_{act} and $\Delta\gamma$ denote the torsional stiffness of the actuator and the angular deflection, respectively, the torque τ of the actuator can be expressed as [29]

$$\tau = K_{act}\Delta\gamma \tag{1}$$

Lead screw transforms the input torque τ to linear force f [30], namely,

$$f = \frac{2\tau}{d_p \tan(\vartheta + \nu)} \tag{2}$$

with

$$\vartheta = \tan^{-1} \frac{l_s}{\pi d_p}; \quad \nu = \tan^{-1} \frac{\mu}{\cos \alpha_t} \tag{3}$$

where d_p and l_s stand for the pitch diameter and the lead of the ball screw, respectively. Moreover, ϑ and ν, respectively, denote the lead angle and friction angle, μ and α_t being the friction coefficient and the radial angle of thread. Moreover, the angular deflection is transformed into linear deformation Δa expressed as

$$\Delta a = l_s \Delta \gamma \tag{4}$$

Combining Eqs. 1, 2, and 4, the actuation stiffness K_a is derived from $f = K_a \Delta a$:

$$K_a = \frac{2K_{act}}{d_p l_s \tan(\vartheta + \nu)} \tag{5}$$

3.1.2 Stiffness matrix of the spatial module

The structure of the spatial module is shown in Fig. 3, of which the stiffness matrix is calculated with the virtual-spring approach. The elastic deformation $\delta \mathbf{b}_{i1}$ of the distal end in the $A_{i1}B_{i1}$ chain can be expressed as:

$$\delta \mathbf{b}_{i1} = \mathbf{J}_{\theta,i1} \delta \theta_{i1} + \mathbf{J}_{q,i1} \delta \mathbf{q}_{i1} \tag{6}$$

where $\mathbf{J}_{\theta,i1}$ is the Jacobian matrix corresponding to the deflections $\delta \theta_{i1}$, and $\mathbf{J}_{q,i1}$ is the Jacobian matrix to consider the small-amplitude angular displacements $\delta \mathbf{q}_{i1}$ of the passive joints, respectively, which are expressed as:

$$\mathbf{J}_{\theta,i1} = \begin{bmatrix} S_u & C_u & 0 & 0 & 0 & 0 \\ -C_u & S_u & 0 & 0 & 0 & 0 \\ 0 & 0 & 1 & 0 & 0 & 0 \\ 0 & 0 & \frac{d}{2} & S_u & C_u & 0 \\ 0 & 0 & 0 & -C_u & S_u & 0 \\ -\frac{dS_u}{2} & -\frac{dC_u}{2} & 0 & 0 & 0 & 1 \end{bmatrix};$$

$$\mathbf{J}_{q,i1} = \begin{bmatrix} C_{qv} & S_{qv}S_t & C_{qv} & S_{qv}S_t \\ 0 & C_t & 0 & C_t \\ -S_{qv} & C_{qv}S_t & -S_{qv} & C_{qv}S_t \\ -\frac{bS_{qv}}{2} & \frac{bC_{qv}S_t}{2} & -\frac{dS_{qv}}{2} & \frac{dC_{qv}S_t}{2} \\ -LS_{qv} & LC_{qv}S_t & 0 & 0 \\ -\frac{bC_{qv}}{2} & -LC_t - \frac{bS_{qv}S_t}{2} & -\frac{dC_{qv}}{2} & -\frac{dS_{qv}S_t}{2} \end{bmatrix} \tag{7}$$

where $C_{qv} = \cos(q + v)$, $S_{qv} = \sin(q + v)$, and the angle t is solved according to the geometric relationship of the module as below [5]

$$t = -2 \tan^{-1} \frac{S_u S_v - \sqrt{C_u^2 + S_u^2 S_v^2}}{C_u} \tag{8}$$

Let the external wrench (six-dimensional array of force and moment) applied to the distal end of $A_{i1}B_{i1}$ chain be $\mathbf{f}_1$, and the force/torque causing the deflection being denoted by τ_1, the equilibrium condition for $A_{i1}B_{i1}$ chain is written as

$$\tau_1 = \mathbf{J}_{\theta,i1}^T \mathbf{f}_1, \quad \tau_1 = \mathbf{K}_L \delta \theta_{i1}, \quad \mathbf{J}_{q,i1}^T \mathbf{f}_1 = \mathbf{0}, \tag{9}$$

and $\mathbf{K}_L$ is the bar-link stiffness matrix, calculated by the Euler–Bernoulli model of a cantilever as shown in Fig. 4, which takes the following form :

$$\mathbf{K}_L = \begin{bmatrix} \frac{GI_x}{L_s} & 0 & 0 & 0 & 0 & 0 \\ 0 & \frac{4EI_y}{L_s}\left(1 + \frac{3h}{L_s} + \frac{3h^2}{L_s^2}\right) & 0 & 0 & 0 & \frac{6EI_y}{L_s^2}\left(1 + \frac{2h}{L_s}\right) \\ 0 & 0 & \frac{4EI_z}{L_s}\left(1 + \frac{3h}{L_s} + \frac{3h^2}{L_s^2}\right) & 0 & -\frac{6EI_z}{L_s^2}\left(1 + \frac{2h}{L_s}\right) & 0 \\ 0 & 0 & 0 & \frac{EA}{L_s} & 0 & 0 \\ 0 & 0 & -\frac{6EI_z}{L_s^2}\left(1 + \frac{2h}{L_s}\right) & 0 & \frac{12EI_z}{L_s^3} & 0 \\ 0 & \frac{6EI_y}{L_s^2}\left(1 + \frac{2h}{L_s}\right) & 0 & 0 & 0 & \frac{12EI_y}{L_s^3} \end{bmatrix} \tag{10}$$

where L_s is the link length, A is its cross-section area, I_y, I_z, and I_x are the quadratic and polar moments of inertia of the cross-section, and E and G are the Young's and shear moduli, respectively. Moreover, the connecting components with length h are considered as rigid.

Combining Eqs. 6 and 9, the kinetostatic model of $A_{i1}B_{i1}$ chain is reduced to

$$\begin{bmatrix} \mathbf{J}_{\theta,i1}\mathbf{K}_L^{-1}\mathbf{J}_{\theta,i1}^T & \mathbf{J}_{q,i1} \\ \mathbf{J}_{q,i1} & \mathbf{0}_2 \end{bmatrix} \begin{bmatrix} \mathbf{f}_1 \\ \delta \mathbf{q}_{i1} \end{bmatrix} = \begin{bmatrix} \delta \mathbf{b}_{i1} \\ \mathbf{0} \end{bmatrix} \tag{11}$$

The stiffness matrix $\mathbf{K}_{\Pi,1}$ of $A_{i1}B_{i1}$ chain in the module is the first five-dimensional entry, as the translational stiffness along z-axis degrades to zero due to the presence of the passive joints, which is extracted for the matrix below [25]:

$$\mathbf{K}'_{\Pi,1} = \begin{bmatrix} \mathbf{J}_{\theta,i1}\mathbf{K}_L^{-1}\mathbf{J}_{\theta,i1} & \mathbf{J}_{q,i1} \\ \mathbf{J}_{q,i1} & \mathbf{0}_2 \end{bmatrix}^{-1} \tag{12}$$

Fig. 3 The structure of the spatial module. **a** Coordinate system. **b** Virtual-spring model

Similarly, the stiffness matrix $\mathbf{K}_{\Pi,2}$ of the chain $A_{i2}B_{i2}$ can be readily found. Subsequently, the stiffness matrix of the spatial module is calculated by a simple addition $\mathbf{K}_{\Pi} = \Sigma_{i=1}^{2}\mathbf{K}_{\Pi,i}$. It should be noted that the rank of $\mathbf{K}_{\Pi}$ is equal to 4 while its size is 5×5, whereas it is available to compute the stiffness matrix of the Biglide parallel mechanism.

3.1.3 Stiffness matrix of the Biglide mechanism

The manipulator under consideration has a serial-parallel structure, as displayed in Fig. 5, of which the Cartesian stiffness matrix $\mathbf{K}$ of the parallel Biglide mechanism is firstly computed. In accordance with Fig. 5, the equilibrium condition of the limb A_1B_1 in Fig. 2b is derived as

$$\$_{P1} = \mathbf{J}_{\theta 1}\delta\boldsymbol{\theta}_1, \quad \boldsymbol{\tau}_1 = \mathbf{J}_{\theta 1}^{T}\mathbf{w}_1, \quad \boldsymbol{\tau}_1 = \mathbf{K}_{\theta}\delta\boldsymbol{\theta}_1 \quad (13)$$

where $\$_{P1}$ is the small-amplitude deformation screw and $\mathbf{w}_1$ is the external wrench exerted on the mobile platform. On the other hand, $\delta\boldsymbol{\theta}_1$ is a vector of the deflections caused by the forces/moments $\boldsymbol{\tau}_1$ in the joint space. Moreover, $\mathbf{J}_{\theta 1}$ and $\mathbf{K}_{\theta}$, respectively, are the Jacobian matrix related to the deflec-

tions and the stiffness matrix in the joint space, expressed as:

$$\mathbf{J}_{\theta 1} = \begin{bmatrix} 0 & C_q & 0 & -S_q & 0 & 0 \\ 0 & 0 & 1 & 0 & 0 & 0 \\ 0 & S_q & 0 & C_q & 0 & 0 \\ 1 & 0 & 0 & 0 & C_q & 0 \\ 0 & rS_q & 0 & rC_q & 0 & 1 \\ 0 & 0 & -r & 0 & S_q & 0 \end{bmatrix}; \quad \mathbf{K}_{\theta} = \begin{bmatrix} K_a C_q & 0 \\ 0 & \mathbf{K}_{\Pi} \end{bmatrix} \quad (14)$$

Consequently, the Cartesian stiffness matrix of limb A_1B_1 is found as $\mathbf{K}_1 = \mathbf{J}_{\theta 1}^{-T}\mathbf{K}_{\theta}\mathbf{J}_{\theta 1}^{-1}$. For limb A_2B_2, the expressions are similar, wherein the Jacobian matrix can be obtained by replacing q with $\pi - q$ and changing the signs of r.

From $\$_P = \$_{Pi}$, $\mathbf{w} = \Sigma_{i=1}^{2}\mathbf{w}_i$, $\mathbf{w}_i = \mathbf{K}_i\$_{Pi}$, $i = 1, 2$, the Cartesian stiffness matrix of the parallel Biglide mechanism is the summation of the stiffness matrices of the two limbs, namely, $\mathbf{K} = \mathbf{K}_1 + \mathbf{K}_2$. With the consideration of the decoupled translation, the Cartesian stiffness matrix of the grinder is rewritten as

$$\mathbf{K}_c = \left(\mathbf{K}^{-1} + K_a^{-1}\mathbf{s}\mathbf{s}^{T}\right)^{-1}; \quad \mathbf{s} = \begin{bmatrix} 0 & 0 & 0 & 0 & 1 & 0 \end{bmatrix}^{T} \quad (15)$$

Fig. 4 The coordinate system of the cantilever of link $A_{i1}B_{i1}$

Fig. 5 The virtual-spring model of the serial-parallel Biglide manipulator

3.2 Decoupling of the stiffness matrix

Decoupling of the Cartesian stiffness matrix is possible if and only if the 3×3 off-diagonal entry is singular [31], which is achieved by means of a similarity transformation that involves only a shift of the origin. As reported in the previous work [5], due to the manipulator architecture, the Cartesian stiffness matrix $\mathbf{K}_c$ in Eq. 15 takes the following form over the reachable workspace:

$$\mathbf{K}_c = \begin{bmatrix} \mathbf{K}_{rr} & \mathbf{K}_{rt} \\ \mathbf{K}_{rt}^T & \mathbf{K}_{tt} \end{bmatrix} = \begin{bmatrix} k_{11} & 0 & 0 & 0 & k_{15} & 0 \\ 0 & k_{22} & 0 & k_{24} & 0 & 0 \\ 0 & 0 & k_{33} & 0 & 0 & 0 \\ 0 & k_{24} & 0 & k_{44} & 0 & 0 \\ k_{15} & 0 & 0 & 0 & k_{55} & 0 \\ 0 & 0 & 0 & 0 & 0 & k_{66} \end{bmatrix} \quad (16)$$

wherefrom it is seen that off-diagonal entry, i.e., $\mathbf{K}_{rt}$, is singular, namely, rank($\mathbf{K}_{rt}$) ≤ 2. This means that the Cartesian stiffness matrix of the Biglide mechanism has the property that it can be decoupled into translational and rotational aspects.

Let the stiffness matrix under study be denoted by $[\mathbf{K}]_{\mathcal{A}}$ when represented in a coordinate frame labeled by $\mathcal{A}$. Similarly, $[\mathbf{K}]_{\mathcal{B}}$ stands for the same matrix in a second frame $\mathcal{B}$, under the assumption that the orientation of the axes and origins of the two frames are different. The matrices $[\mathbf{K}]_{\mathcal{A}}$ and $[\mathbf{K}]_{\mathcal{B}}$ are displayed below:

$$[\mathbf{K}]_{\mathcal{A}} = \begin{bmatrix} \mathbf{K}_{rr} & \mathbf{K}_{rt} \\ \mathbf{K}_{rt}^T & \mathbf{K}_{tt} \end{bmatrix}; \quad [\mathbf{K}]_{\mathcal{B}} = \begin{bmatrix} \mathbf{K}'_{rr} & \mathbf{K}'_{rt} \\ \mathbf{K}'^T_{rt} & \mathbf{K}'_{tt} \end{bmatrix} \quad (17)$$

Thus, the coordinate transformation that relates $[\mathbf{K}]_{\mathcal{A}}$ with $[\mathbf{K}]_{\mathcal{B}}$ between different reference frames $\mathcal{A}$ and $\mathcal{B}$ [32] can be derived readily as

$$[\mathbf{K}]_{\mathcal{B}} = \Gamma \mathbf{S} \Gamma^{-1} [\mathbf{K}]_{\mathcal{A}} \mathbf{S}^{-1} \quad (18)$$

with the 6×6 permutation matrix Γ defined in its block form as below

$$\Gamma = \begin{bmatrix} \mathbf{O} & \mathbf{I} \\ \mathbf{I} & \mathbf{O} \end{bmatrix} \quad (19)$$

where $\mathbf{I}$ is the 3D identity matrix and $\mathbf{O}$ is the 3D zero matrix. And

$$\mathbf{S} = \begin{bmatrix} \mathbf{Q} & \mathbf{O} \\ \mathbf{DQ} & \mathbf{Q} \end{bmatrix}; \quad \Gamma \mathbf{S} \Gamma^{-1} = \Gamma \mathbf{S} \Gamma = \begin{bmatrix} \mathbf{Q} & \mathbf{DQ} \\ \mathbf{O} & \mathbf{Q} \end{bmatrix} \quad (20)$$

where $\mathbf{Q}$ denotes the rotation matrix from the frame $\mathcal{B}$ to $\mathcal{A}$, while $\mathbf{D}$ is the cross-product matrix (CPM) of the displacement $\mathbf{d}$ that carries the origin of frame $\mathcal{B}$ into that of $\mathcal{A}$, defined as $\mathbf{D} = \text{CPM}(\mathbf{d})$ [33].

The expanded form of the congruence transformation (18) of spatial stiffness can be given by

$$\mathbf{K}'_{rr} = \mathbf{Q}(\mathbf{K}_{rr} - \mathbf{K}_{rt}\mathbf{D})\mathbf{Q}^T + \mathbf{DQ}(\mathbf{K}_{rt}^T - \mathbf{K}_{tt}\mathbf{D})\mathbf{Q}^T \quad (21a)$$

$$\mathbf{K}'_{rt} = (\mathbf{Q}\mathbf{K}_{rt} + \mathbf{DQ}\mathbf{K}_{tt})\mathbf{Q}^T \quad (21b)$$

$$\mathbf{K}'_{tt} = \mathbf{Q}\mathbf{K}_{tt}\mathbf{Q}^T \quad (21c)$$

Under the decoupling condition $\mathbf{K}'_{rt} = \mathbf{O}$, matrix $\mathbf{Q}$ can be freely chosen as the identity matrix $\mathbf{I}$, which yields

$$\mathbf{K}'_{rr} = \mathbf{K}_{rr} - \mathbf{K}_{rt}\mathbf{D} + \mathbf{D}(\mathbf{K}_{rt}^T - \mathbf{K}_{tt}\mathbf{D}) \quad (22a)$$

$$\mathbf{DK}_{tt} = -\mathbf{K}_{rt} \quad (22b)$$

$$\mathbf{K}'_{tt} = \mathbf{K}_{tt} \quad (22c)$$

whence $\mathbf{D}$, a 3×3 skew-symmetric matrix, can be determined from Eq. 22b, hence, rank($\mathbf{DK}_{tt}$) ≤ 2, in accordance with Sylvester's theorem [34]. Under the assumption that $\mathbf{K}_{rt}$ is singular, $\mathbf{D}$ is found upon taking the axial vector [33] of both sides of Eq. 22b, namely,

$$\mathbf{Md} = \text{vect}(\mathbf{K}_{rt}); \quad \mathbf{M} = \frac{1}{2}[\text{tr}(\mathbf{K}_{tt})\mathbf{I} - \mathbf{K}_{tt}] \quad (23)$$

where $\mathbf{M}$ carries unit N/m and tr($\mathbf{K}_{tt}$) is the trace of $\mathbf{K}_{tt}$. Operation vect($\cdot$) is the mapping from skew-symmetric matrix to its corresponding vector. If $\mathbf{M}$ is invertible, then $\mathbf{d} = \mathbf{M}^{-1}\text{vect}(\mathbf{K}_{rt})$; otherwise, $\mathbf{M}$ fails to be invertible, but $\mathbf{d}$ can still be calculated [31].

Upon the decoupled translational and rotational stiffness matrices, the max-/minimum translational and rotational stiffnesses can be identified by virtue of the eigenvalue problem, where the eigenvalues are considered as the principal stiffnesses. The minimum eigenvalues of the translational and rotational stiffness matrices are then defined as the translational and rotational stiffness performance indices, namely,

$$\kappa_t = \min(\lambda_i), \quad \kappa_r = \min(\sigma_i); \quad i = 1, 2, 3 \quad (24)$$

where λ_i and σ_i, respectively, are the eigenvalues of translational and rotational stiffness matrices $\mathbf{K}'_{tt}$ and $\mathbf{K}'_{rr}$. These indices can be used in either performance evaluation or optimum design. The larger the indices, the higher the rigidity of the manipulator. As the stiffness analysis plays a significant role in the manipulator design, the decoupling of stiffness matrix can be applied in this process, through which parameters and dimensions are evaluated to optimize the manipulator performance.

4 Design optimization of the Biglide machine

This work aims to modify the link lengths of the Biglide parallel grinder with high translational and rotational stiffnesses throughout an increased regular dexterous workspace. The foregoing defined stiffness indices can be applied in the optimization procedure to obtain a design with optimal elastostatic performance. Besides, the kinematic performances are taken into account as constraints to guarantee the manipulability over the designated workspace.

4.1 Design variables

The manipulator performance heavily depends on the geometry and link properties. In this design, the link is made of the selected composite carbon fiber tube for lightweight and stiff design, and the connecting components at both ends are manufactured by alloy aluminum with a constant length for light weight. As a consequence, the design variables of the optimization problem at hand are:

$$\mathbf{x} = \begin{bmatrix} L_0 & r & b & d \end{bmatrix}^T \tag{25}$$

4.2 Optimization objectives

Aiming to make the redesigned mechanism to have high stiffness, the foregoing defined indices κ_t and κ_r should be maximized; consequently, the first two objective functions are written as :

$$f_1(\mathbf{x}) = \kappa_t \quad \rightarrow \quad \max \tag{26a}$$

$$f_2(\mathbf{x}) = \kappa_r \quad \rightarrow \quad \max \tag{26b}$$

On the other hand, in order for the mechanism to be compact, the third objective function is written as:

$$f_3 = b \quad \rightarrow \quad \min \tag{27}$$

4.3 Optimization constraints

To make the mechanism have a better motion/force transmission within a specified rectangular workspace $w_x \times w_z$, w_x and w_z being the length and height of the rectangle, the input β and output γ transmission angles should be greater than a value η, as shown in Fig. 6, namely,

$$\sin \beta = \cos q \geq \sin \eta = \cos q_{\max};$$

$$\sin \gamma = \sin q \geq \sin \eta = \sin q_{\min} \tag{28}$$

or

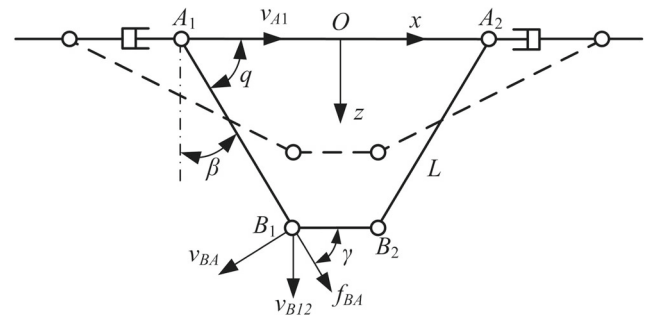$$\sin^{-1}(\sin \eta) \leq q \leq \cos^{-1}(\sin \eta) \tag{29}$$

Fig. 6 The transmission angles of the Biglide parallel mechanism

where $[q_{\min}, q_{\max}]$ represents the range of angle q for better transmission quality. Thus, the constraint on the link length is written as:

$$L(\sin q_{\max} - \sin q_{\min}) \geq w_z \tag{30}$$

4.4 Formulation of the multi-objective optimization problem

Mathematically, the multi-objective optimization problem (MOOP) for the Biglide parallel mechanism is formulated as:

$$
\begin{aligned}
\text{maxmize} \quad & f_1(\mathbf{x}) = \kappa_t \\
\text{maxmize} \quad & f_2(\mathbf{x}) = \kappa_r \\
\text{minimize} \quad & f_3 = b \\
\text{over} \quad & \mathbf{x} = \begin{bmatrix} L_0 & r & b & d \end{bmatrix}^T \\
\text{subject to} \quad & g_1 : \sin^{-1}(\sin \eta) \leq q \leq \cos^{-1}(\sin \eta) \\
& g_2 : L(\sin q_{\max} - \sin q_{\min}) \geq w_z \\
& g_3 : L_0^2 = L^2 + (b/2 - d/2)^2
\end{aligned} \tag{31}
$$

5 Results and discussion

The optimization procedure is applied to the Biglide mechanism shown in Fig. 2a for an increased workspace size $w_x = 2w_z = 500$ mm. The actuation inherits from the original machine with larger length of the ball screw to increase the motion range of the sliding units, of which the parameters are listed in Table 1 together with the link properties. With the consideration of the avoidance of mechanical collision and architecture compactness, the lower and upper bounds of the design variables, denoted by $\mathbf{x}_{lb}$ and $\mathbf{x}_{ub}$, respectively, are given by:

$$\mathbf{x}_{lb} = \begin{bmatrix} 680 & 70 & 250 & 150 \end{bmatrix}^T ; \quad \mathbf{x}_{ub} = \begin{bmatrix} 700 & 100 & 400 & 200 \end{bmatrix}^T \tag{32}$$

Table 1 The actuation parameters and link properties of the Biglide parallel grinder

Lead screw system					Link L_0			
K_{act} [Nm/rad]	d_p [mm]	l_s [mm]	μ	α_t [deg]	Fiber tube	h [mm]	E [GPa]	G [GPa]
10^3	16	20	0.01	15	Ø60/54 mm	100	110	42.3

Moreover, the most widely accepted transmission angle is $90 \pm 45°$ for high-quality transmission in the literature [35]. Henceforth, let the transmission angle be $\sin \eta = \sin \beta \sin \gamma = (\sin 45°)^2 = \sin 30°$; the range of q for better transmission quality is: $q_{min} = 30°$, $q_{max} = 60°$.

5.1 Pareto front of the optimization problem

The solutions of the previous optimization problem are non-dominated solutions, also called Pareto optimal solutions or Pareto front. Problem (31) is solved by the genetic algorithm NSGA-II [36], a stochastic and time-demanding procedure, for which the algorithm parameters are given in Table 2.

The evolutionary Pareto front of the MOOP (31) is illustrated in Fig. 7, and the Pareto optimal solutions after 1000 generations are displayed in Fig. 8. With *plotmatrix* and *corrcoef* functions in Matlab^{TM}, one obtains the scatter matrix to illustrate the variational trends as well as the interdependency between the objective functions and design variables, as displayed in Fig. 9. The lower triangular part of the matrix represents the correlation coefficients whereas the upper one shows the corresponding scatter plots. The diagonal elements represent the probability density charts of each variable. The correlation coefficients vary from -1 to 1, and two variables are strongly dependent when their correlation coefficient is close to -1 or 1 and independent when the latter is null. Figure 9 shows that:

- Linear κ_t and rotational κ_r stiffnesses are strongly dependent as their correlation coefficient is equal to -0.972, whereas they are antagonistic
- Both κ_t and κ_r are strongly dependent on the design variables L_0, b, and d, while r does not have significant influence to the stiffness
- All the variables are strongly dependent on each other except r

Table 2 Algorithm parameters of the implemented NSGA-II

Population size	Number of generations	Directional crossover probability	Crossover probability	Distribution index
100	1000	0.5	0.95	20

- The larger L_0, b and smaller d, the higher κ_t, conversely, the lower κ_r
- Variable r in most populations converges to its lower bound

5.2 Analysis of the selected design

The working condition of the Biglide machine is that the end-effector usually bears external forces; thus, the design with $\max(\kappa_t)$ on the Pareto front in Fig. 8 is selected, of which the design variables are $L_0 = 695 \, \text{mm} \, (L = 684)$, $r = 76 \, \text{mm}$, $b = 400 \, \text{mm}$, and $d = 150 \, \text{mm}$. The corresponding CAD model is shown in Fig. 10 as well as the workspace in Fig. 11, where points $P1$ and $P2$ are considered as the representative workspace points because of the symmetrical configuration of the mechanism.

At position $P1$, the Cartesian stiffness matrix of the Biglide parallel mechanism is computed as

$$\mathbf{K}_c = \begin{bmatrix} \mathbf{K}_{rr} & \mathbf{K}_{rt} \\ \mathbf{K}_{rt}^T & \mathbf{K}_{tt} \end{bmatrix}$$

$$= \begin{bmatrix} 0.106 & 0 & 0 & 0 & -0.158 & 0 \\ 0 & 1.039 & 0 & -3.501 & 0 & 0 \\ 0 & 0 & 0.136 & 0 & 0 & 0 \\ 0 & -3.501 & 0 & 26.408 & 0 & 0 \\ -0.158 & 0 & 0 & 0 & 0.771 & 0 \\ 0 & 0 & 0 & 0 & 0 & 176.441 \end{bmatrix} \cdot 10^6 \quad (33)$$

where the entries $\mathbf{K}_{rr}$, $\mathbf{K}_{rt}$, and $\mathbf{K}_{tt}$ are given in Nm, N, and N/m, respectively.
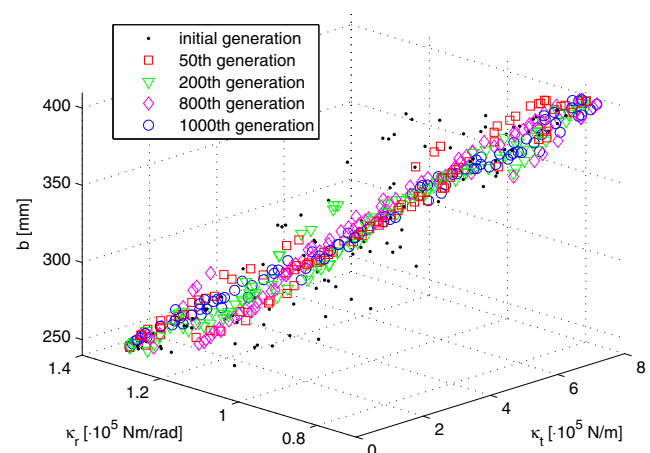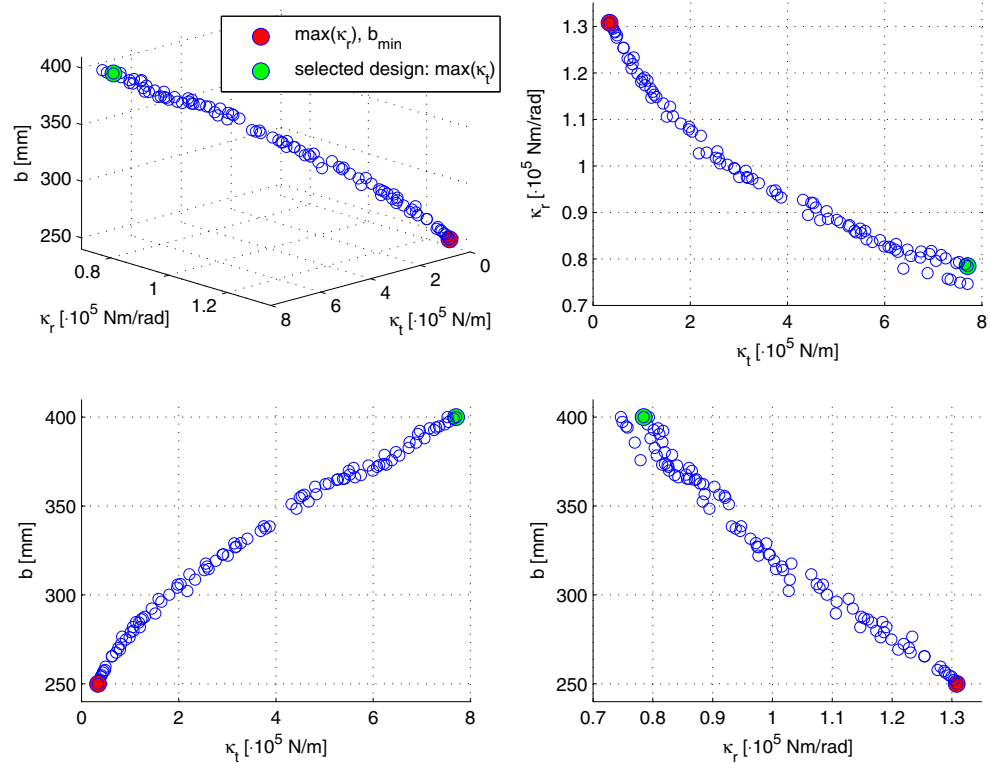

Fig. 7 The evolutionary Pareto-front of the MOOP (31)

Fig. 8 The Pareto front of the MOOP (31) obtained after 1000 generations

In the decoupling of the stiffness matrix (33), matrix $\mathbf{M}$ in Eq. 23 is computed as

$$\mathbf{M} = \text{diag} \begin{bmatrix} 0.886 & 1.014 & 0.136 \end{bmatrix} \cdot 10^8 \, \text{N/m} \tag{34}$$

which is invertible; consequently, $\mathbf{d}$ follows the simple inversion of $\mathbf{M}$:

$$\mathbf{d} = \begin{bmatrix} 0 & 0 & -0.123 \end{bmatrix}^T \, \text{m} \tag{35}$$

Following the relation $\mathbf{D} = \text{CPM}(\mathbf{d})$, one obtains

$$\mathbf{D} = \begin{bmatrix} 0 & 0.123 & 0 \\ -0.123 & 0 & 0 \\ 0 & 0 & 0 \end{bmatrix} \, \text{m} \tag{36}$$

Substituting matrix $\mathbf{D}$ into Eqs. 22a and 22c, $\mathbf{K}'_{rr}$ and $\mathbf{K}'_{tt}$ are calculated as

$$\mathbf{K}'_{rr} = \text{diag} \begin{bmatrix} 0.079 & 2.300 & 0.136 \end{bmatrix} \cdot 10^6 \, \text{Nm};$$

$$\mathbf{K}'_{tt} = \text{diag} \begin{bmatrix} 26.408 & 0.771 & 176.441 \end{bmatrix} \cdot 10^6 \, \text{N/m} \tag{37}$$

Matrix $\mathbf{K}_c$ now is decoupled into two homogeneous submatrices corresponding to the translational and rotational stiffnesses; thus, resorting to the eigenvalue problem, one can identify the directions along which the max-/minimum

Fig. 9 Scatter matrix for the objective functions and the design variables

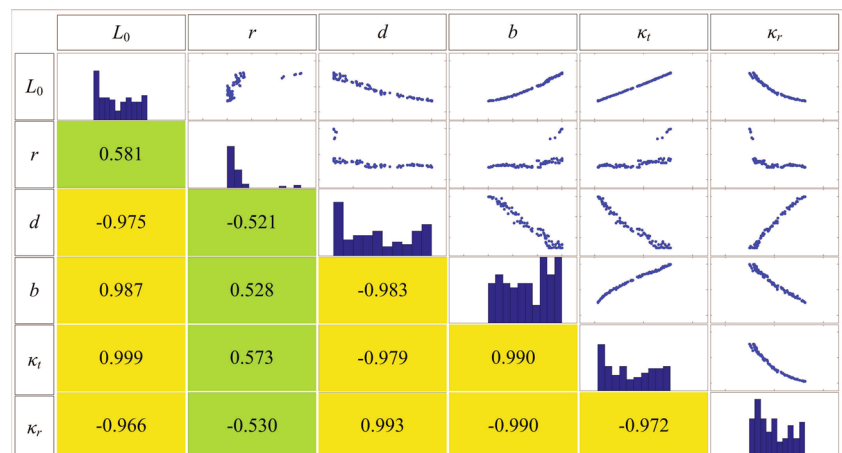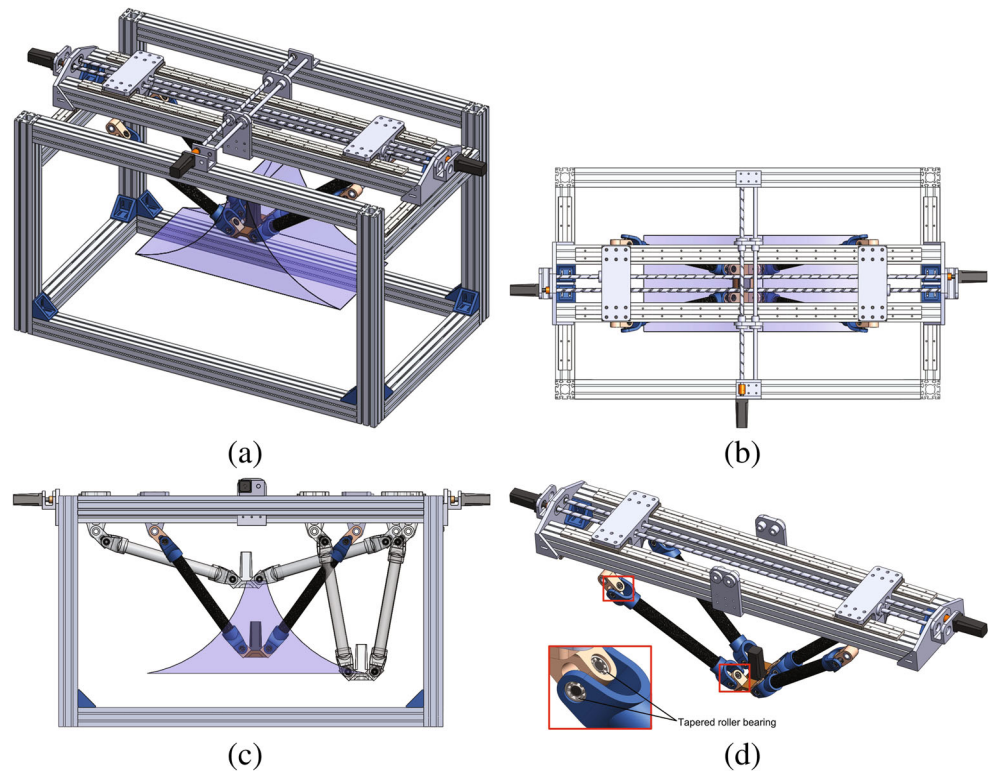|	L_0	r	d	b	κ_t	κ_r
L_0						
r	0.581					
d	-0.975	-0.521				
b	0.987	0.528	-0.983			
κ_t	0.999	0.573	-0.979	0.990		
κ_r	-0.966	-0.530	0.993	-0.990	-0.972	

Fig. 10 The CAD model of the Biglide parallel grinder. **a** Isometric view. **b** Top view. **c** Front view. **d** The planar Biglide mechanism

principal stiffness exists. Similarly, matrices $\mathbf{K}'_{tt}$ and $\mathbf{K}'_{rr}$ at position $P2$ are found as:

$$\mathbf{K}'_{rr} = \text{diag} \begin{bmatrix} 1.572 & 2.690 & 0.868 \end{bmatrix} \cdot 10^5 \, \text{Nm};$$

$$\mathbf{K}'_{tt} = \text{diag} \begin{bmatrix} 15.274 & 0.771 & 37.562 \end{bmatrix} \cdot 10^6 \, \text{N/m} \tag{38}$$

It is noteworthy that the entries $\mathbf{K}'_{tt}$ and $\mathbf{K}'_{rr}$ are diagonal; thus, the diagonal elements of each matrix indicate the principal translational and rotational stiffnesses. Let λ_x, λ_y, λ_z, and σ_x, σ_y, σ_z denote the diagonal elements of matrices $\mathbf{K}'_{tt}$ and $\mathbf{K}'_{rr}$, respectively; their values depend on the z-coordinates, as shown in Fig. 12a. It is observed that the machine has significantly higher translational stiffness λ_z in z-direction, one and two orders of magnitude larger than λ_x and λ_y, respectively. The translational stiffness λ_y in the

y-direction, being the smallest translational stiffness, remains constant. In addition, the rotational stiffness σ_y around y-axis is one order of magnitude larger than the other two rotational stiffnesses. Moreover, the principal stiffnesses except σ_x and λ_y become smaller with the increasing z-coordinates.

To evaluate the elastostatic performance of the Biglide machine, a reasonable thrust force 500 N and a torque 5 Nm in the drilling operation [37] are applied to the end-effector, and the corresponding angular $\|\delta\phi\|$ and linear $\|\delta\mathbf{p}\|$ deflections are calculated and shown in Fig. 12b, from which it is seen that the elastic deformations are quite small. Unlike cutting material in the drilling operation, the forces and torques during grinding process are much smaller, resulting in even smaller deformations. This means that the modified machine still has high structural stiffness to meet

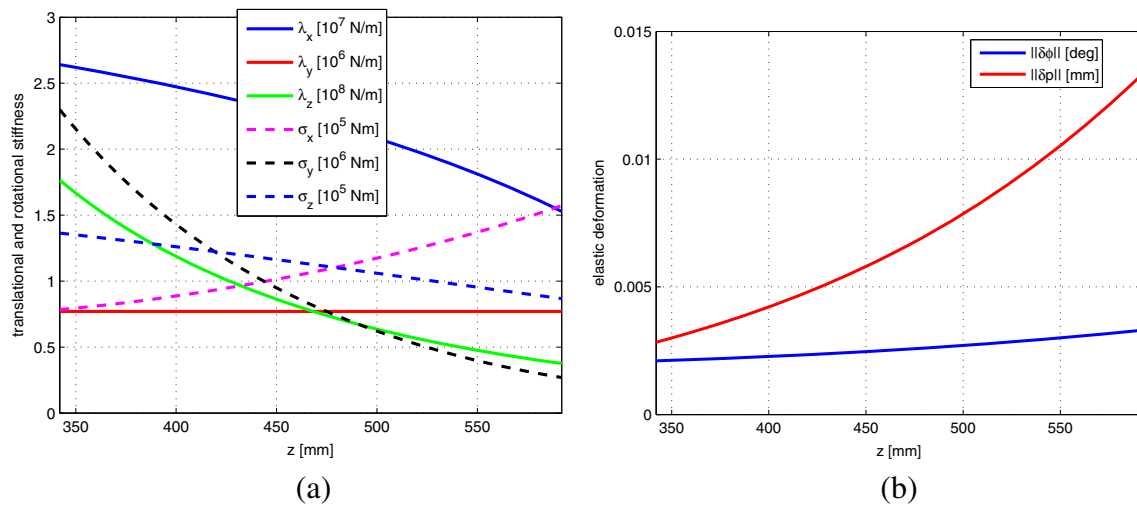**Fig. 11** The workspace of the optimized Biglide parallel grinder
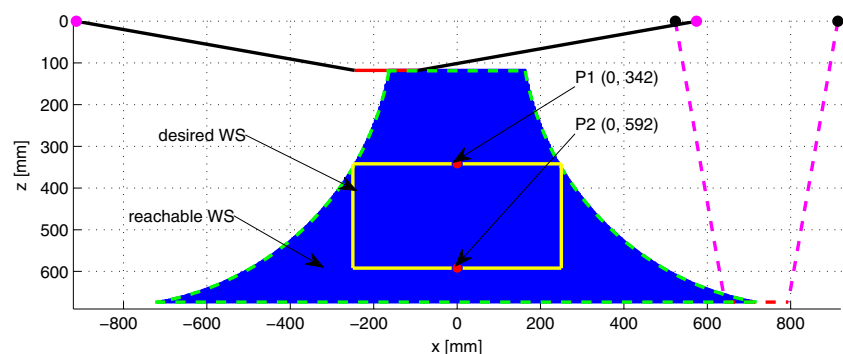
Fig. 12 Stiffness behaviors of the optimized Biglide grinder. **a** Translational and rotational stiffness with respect to *z*-coordinates. **b** Elastic deformations in a drilling operation

the requirement of accuracy as a drill grinding machine. Moreover, the total weight of the spatial modules is close to that of the original design with increased link length.

6 Conclusions

This paper dealt with the optimal structural design of a Biglide parallel grinder for grinding drill point. A pair of spatial modules, composed of composite carbon tube for lightweight design, was adopted to replace the conventional parallelogram to enhance the out-of-plane stiffness of the latter. The Cartesian stiffness matrix of the Biglide machine was modeled and further used in the design optimization procedure. A multi-objective design optimization problem was formulated in order to determine the mechanism optimum structural parameters. Performance evaluation criteria, including stiffness, motion/force transmission, and workspace, were taken into consideration. The Pareto front of the multi-objective optimization problem was obtained to provide the optimum design of the Biglide machine, and a scatter matrix was visualized to reveal the influence of the link dimensions to the performance as well as the mutual dependency of the performance measures. An optimal solution with the maximal translational stiffness from the Pareto front was selected for the redesign of the Biglide machine, which can guarantee the requirement on the elastostatic performance in the grinding process with increased dexterous workspace size.

References

1. Yan L, Jiang F (2013) A practical optimization design of helical geometry drill point and its grinding process. Int J Adv Manuf Technol 64(9–12):1387–1394
2. Zou P (2003) Kinematic analysis of a Biglide parallel grinder. J Mater Process Technol 138(1–3):461–463
3. Li B, Hu Y, Wang H (2007) Analysis and simulation for a parallel drill point grinder, part 2: grinding kinematic modeling and simulation. Int J Adv Manuf Technol 31(9–10):915–925
4. Zou P, Yang XL, Ai MZ (2010) Study on helical drill point grinding with a Biglide parallel grinder. Adv Mater Res 97:2119–2122
5. Wu G, Zou P (2016) Stiffness analysis and comparison of a Biglide parallel grinder with alternative spatial modular parallelograms. Robotica FirstView:1–17
6. Wenger P, Chablat D (2000) Kinematic analysis of a new parallel machine tool: the Orthoglide. In: Advances in robot kinematics. Springer, pp 305–314
7. Stamper RE, Tsai L-W, Walsh GC (1997) Optimization of a three DOF translational platform for well-conditioned workspace. In: IEEE international conference on robotics and automation, vol 4. IEEE, pp 3250–3255
8. Merlet J-P (2006) Jacobian, manipulability, condition number, and accuracy of parallel robots. J Mech Des 128(1):199–206
9. Huang T, Zhao X, Whitehouse DJ (2002) Stiffness estimation of a tripod-based parallel kinematic machine. IEEE Trans Robot Autom 18(1):50–58
10. Hay AM, Snyman JA (2004) Methodologies for the optimal design of parallel manipulators. Int J Numer Methods Eng 59(1):131–152
11. Chablat D, Caro S, Ur-Rehman R, Wenger P (2010) Comparison of planar parallel manipulator architectures based on a multi-objective design optimization approach. In: ASME 2010 international design engineering technical conferences and computers and information in engineering conference. Montreal, pp 861–870
12. Stock M, Miller K (2003) Optimal kinematic design of spatial parallel manipulators: application to linear Delta robot. J Mech Des 125(2):292–301

13. Hao F, Merlet J-P (2005) Multi-criteria optimal design of parallel manipulators based on interval analysis. Mech Mach Theory 40(2):157–171

14. Krefft M, Hesselbach J (2005) Elastodynamic optimization of parallel kinematics. In: IEEE international conference on automation science and engineering, pp 357–362

15. Altuzarra O, Hernandez A, Salgado O, Angeles J (2009) Multiobjective optimum design of a symmetric parallel Schönflies-motion generator. J Mech Des 131(3):031002

16. Ur-Rehman R, Caro S, Chablat D, Wenger P (2010) Multiobjective path placement optimization of parallel kinematics machines based on energy consumption, shaking forces and maximum actuator torques: application to the orthoglide. Mech Mach Theory 45(8):1125–1141

17. Wu G, Caro S, Bai S, Kepler J (2014) Dynamic modeling and design optimization of a 3-DOF spherical parallel manipulator. Robot Auton Syst 62(10):1377–1386

18. Huo D, Cheng K, Wardle F (2010) Design of a five-axis ultra-precision micro-milling machine–UltraMill. part 1: holistic design approach, design considerations and specifications. Int J Adv Manuf Technol 47(9):867–877

19. Huo D, Cheng K, Wardle F (2010) Design of a five-axis ultra-precision micro-milling machine—UltraMill. Part 2: integrated dynamic modelling, design optimisation and analysis. Int J Adv Manuf Technol 47(9):879–890

20. Germain C, Caro S, Briot S, Wenger P (2013) Singularity-free design of the translational parallel manipulator IRSBot-2. Mech Mach Theory 64:262–285

21. Gosselin C (1990) Stiffness mapping for parallel manipulators. IEEE Trans Robot Autom 6(3):377–382

22. Chen S-F, Kao I (2000) Conservative congruence transformation for joint and cartesian stiffness matrices of robotic hands and fingers. Int J Robot Res 19:835–847

23. Alici G, Shirinzadeh B (2005) Enhanced stiffness modeling, identification and characterization for robot manipulators. IEEE Trans Robot 21(4):554–564

24. Majou F, Gosselin C, Wenger P, Chablat D (2007) Parametric stiffness analysis of the Orthoglide. Mech Mach Theory 42 (3):296–311

25. Pashkevich A, Chablat D, Wenger P (2009) Stiffness analysis of overconstrained parallel manipulators. Mech Mach Theory 44(5):966–982

26. Nagai K, Liu Z (2008) A systematic approach to stiffness analysis of parallel mechanisms. In: IEEE international conference on robotics and automation, pp 1543–1548

27. Klimchik A, Furet B, Caro S, Pashkevich A (2015) Identification of the manipulator stiffness model parameters in industrial environment. Mech Mach Theory 90:1–22

28. Wu G, Bai S, Kepler J (2014) Mobile platform center shift in spherical parallel manipulators with flexible limbs. Mech Mach Theory 75:12–26

29. Wang D, Fan R, Chen W (2013) Stiffness analysis of a hexaglide parallel loading mechanism. Mech Mach Theory 70:454–473

30. Shigley JE, Mischke CR, Brown TH (2004) Standard handbook of machine design. McGraw-Hill

31. Angeles J (2010) On the nature of the Cartesian stiffness matrix. Ingeniería Mecánica 3(5):163–170

32. Roberts RG (2002) On the normal form of a spatial stiffness matrix. In: Proceedings of IEEE international conference on robotics and automation, vol 1, pp 556–561

33. Angeles J (2007) Fundamentals of robotic mechanical systems: theory, methods, and algorithms. Springer, New York

34. Strang G (2005) Linear algebra and its applications, 4th edn. Cengage Learning

35. Tao DC (1964) Applied linkage synthesis. Addison-Wesley, Reading

36. Deb K, Pratap A, Agarwal S, Meyarivan T (2002) A fast and elitist multiobjective genetic algorithm: NSGA-II. IEEE Trans Evol Comput 6(2):182–197

37. Paul A, Kapoor SG, DeVor RE (2005) Chisel edge and cutting lip shape optimization for improved twist drill point design. Int J Mach Tools Manuf 45(4):421–431